

<sup>1</sup> PREPARED FOR SUBMISSION TO JINST

<sup>2</sup> **Directional Xenon Measurement**

---

<sup>3</sup> ABSTRACT: Abstract...

<sup>4</sup> KEYWORDS: Only keywords from JINST's keywords list please

<sup>5</sup> ARXIV EPRINT: [1234.56789](https://arxiv.org/abs/1234.56789)

---

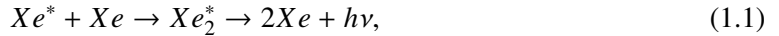
<b>6</b>	<b>Contents</b>		
<b>7</b>	<b>1</b>	<b>Introduction</b>	<b>1</b>
<b>8</b>	<b>2</b>	<b>Experimental Setup</b>	<b>2</b>
9	2.1	The Gas Handling System	3
10	2.2	The Cryogenic System	4
11	2.3	The Detector System	6
12	2.4	The data acquisition system	7
13	2.5	The slow control system	9
<b>14</b>	<b>3</b>	<b>Optical Properties of the Sphere</b>	<b>9</b>
<b>15</b>	<b>4</b>	<b>Detector sensitivity</b>	<b>10</b>
<b>16</b>	<b>5</b>	<b>Commissioning runs</b>	<b>12</b>
17	5.1	Stability Runs	13
18	5.2	Time resolution	13
<b>19</b>	<b>6</b>	<b>Summary</b>	<b>13</b>

---

## 20 **1 Introduction**

21 The use of Noble-liquid detectors in the field of astroparticle physics has increased in the past  
22 decades. Detectors aiming at measuring Dark Matter (DM) particles and neutrinos properties use  
23 large liquid argon or liquid xenon (LXe) chambers [1, 2]. Current and future experiment for DM  
24 detectioin are tuned to detect weakly interacting massive particles (WIMPs), a postulated candiadte  
25 for DM particle [3]. LXe based detectors are to date the leading in sensitivity and size for these  
26 searches [4–7].

27 When a particle interacts within the LXe media, it forms a cloud of excited and ionized states  
28 with typical length of 100 nm. The excited Xe ( $Xe^*$ ) combines with other Xe atoms to form an  
29 excited dimer state (excimer) when they decay to ground state they emit light.



30 The electrons emitted from the ionization can recombine with a surrounding atom, this process of  
31 recombination provides another possibility to produce excimers,



Once  $Xe^*$  is produced it adds to the scintillation process explained in 1.1. There are two types of  $Xe_2^*$  excimer states, singlet and triplet, with lifetime of  $\sim 3$  ns and  $\sim 25$  ns respectively. The wavelength emitted by these states is between (175-180) nm which is lower than the lowest excitation of xenon, and therefore travel through it to reach a photo-detector situated outside the LXe. Although much is measured on these scintillation processes, the basic knowledge of the quantum properties of these interactions is based on experiments preformed several decades ago.

The phenomenon of superradiance in which identical quantum states "communicate" through electromagnetic field if in close proximity, is well studied. In certain conditions the emission of photons from these correlated states is very different than the sum of random states. This difference is in spectral, temporal and spatial properties [8, 9]. Early studies show that scintillation in LXe can produce coherent amplification of light [10, 11]. These studies were focusing on the macroscopic ionization using high energy density electron beams.

The understanding and quantification of the microscopic effects of non linear phenomena such as superradiance in Lxe for a single interaction, can improve DM experiments to reduce background by the extra knowledge of directionality. irreducible background such as coherent neutrino nucleus scattering of neutrinos from the sun can be discard.

In this paper we present an experimental set-up called DIREXENO (DIREctional XENOn) at some places later, DIREXENO is called as Direxeno/DireXeno etc. Please make it a uniform throughout aiming at measuring the spatial distribution of LXe scintillation light, and quantify non-isotropic emission.

## 2 Experimental Setup

In order to identify *superradiance* effects in LXe, the temporal and spatial properties of scintillation events should be studied and quantified. In the DIREXENO system LXe is circulated through a small spherical cavity held in a thick sphere made of high purity fused silica (HPFS). The sphere is surrounded ( $\sim 4\pi$ ) by PMTs allowing high resolution, both spatial and temporal, measurements of individual photons. The PMTs do not come in contact with the xenon, so less impurities are introduced to it, and the material selection is less stringent. The geometrical design of the system approximates a point source of scintillation photons, and a detailed vertex reconstruction within the LXe bubble is unnecessary. A schematic view of the system is shown in Fig 1 .

The current system is designed with  $\sim 1$  ns time resolution, less than 1 ns synchronization between PMTs, and  $\sim 0.8$  radians spatial resolution. Since the exact nature and magnitude of *superradiance* in LXe is yet unknown a guiding principle in the design was flexibility to upgrades or redesign of any part of the system to fulfill any future experiment requirements. The modular design allows fast and easy recovery in case of components malfunction.

The system is made of four main building blocks. (i) **The gas handling system** which in normal working mode circulates the xenon and purifies it. (ii) **The cryogenic system**, liquefies the xenon and delivers it to the detector system. (iii) **The detector system** consists of an HPFS sphere that holds a small bubble of LXe target, and PMTs around it. (iv) **The DAQ system** supplies High Voltage (HV) to the PMTs and handles monitoring, triggering and digitization of data. The entire assembly is held on 3 separate racks as shown in Fig. 2.

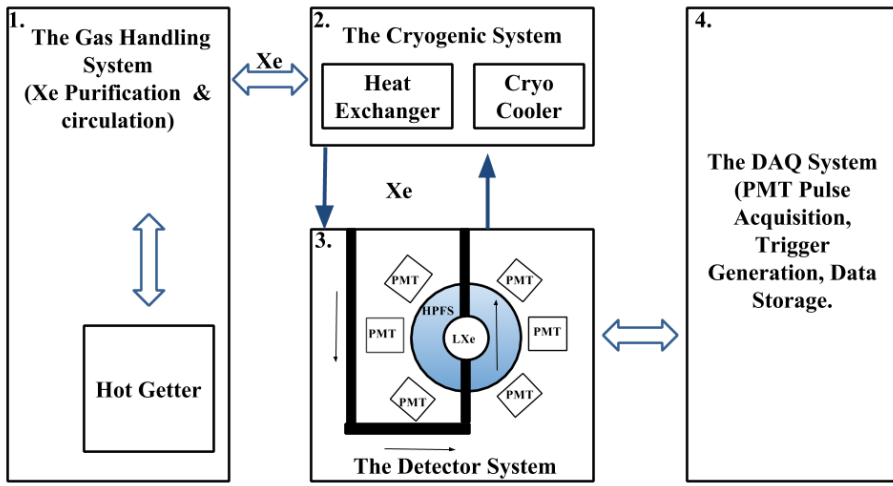


**Figure 1.** A schematic view of DireXeno.

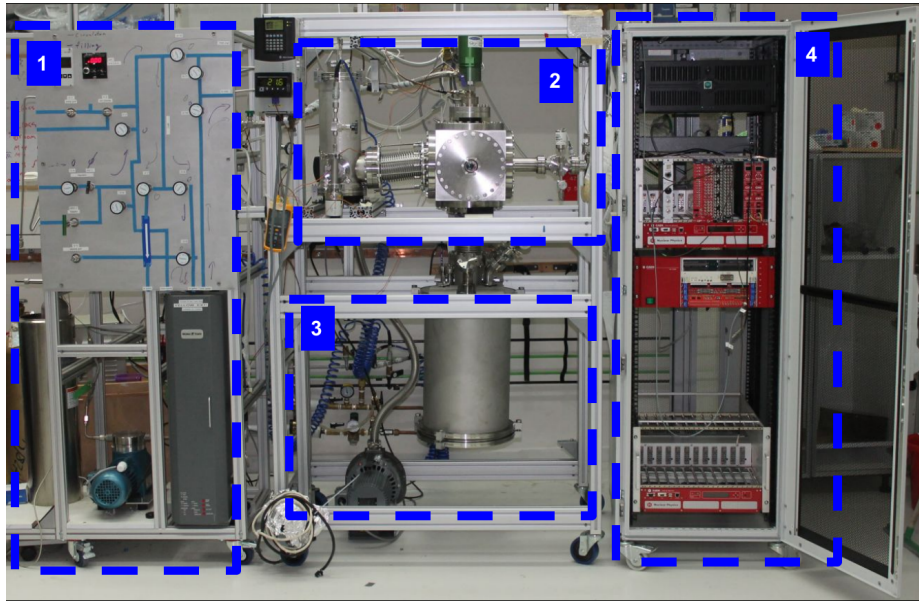


**Figure 2.** The DIREXENO system mounted on the three racks. 1. The gas handling system. 2. The cryogenic system including the heat exchanger. 3. The detector chamber. 4. The Data acquisition system.

## 72    2.1 The Gas Handling System

73    In DIREXENO, only the prompt scintillation is measured, so a high level of LXe purity is not of a  
 74    great importance. However in many LXE detectors the desired level of impurity concentration is

75 at the level of 1 ppb O<sub>2</sub> equivalent [1], this is crucial to allow ionization electrons drift for several  
 76 cm. To reach that purity level in a reasonable amount of time (several days instead of months), a  
 77 continuous purification is needed. The gas handling system provides this process along with all gas  
 78 handling operations such as filling, recuperation and circulation. The xenon circulation also plays  
 79 a major role in heat transfer.

80 During purification, The xenon is forced by a circulation pump<sup>1</sup> extracting LXe from the de-  
 81 tector part through a heat exchanger<sup>2</sup>, where it is heated and vaporized, into a hot getter<sup>3</sup> which  
 82 cleans the xenon. The xenon passes through a mass flow controller<sup>4</sup> (MFC), enabling monitoring  
 83 and controlling the amount of heat introduced to the system. Once purified, the xenon is delivered  
 84 back to the cryogenic system via the heat exchanger, where the remaining GXe is liquefied before  
 85 flowing back to the detector part. A schematic of this system is shown in fig. 3.

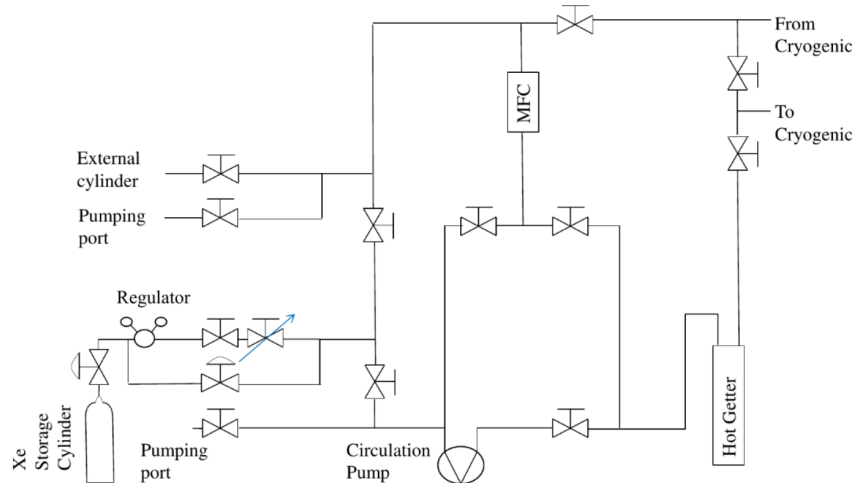


**Figure 3.** Schematics of the gas handling system. High pressure valves are indicated as valves with arcs. Needle valves are indicated as a valve with an arrow.

## 86 2.2 The Cryogenic System

87 Remote cooling is generally used in LXe experiments due to reduction in background radiation and  
 88 acoustic noise from the cooler to the detector, and due to design flexibility. The cryogenic system  
 89 is connected to the gas handling system on one side and to the detector part on the other, and built  
 90 such that replacing the cryo-cooler type (e.g., to PTR) requires just an adaptation to the top flange.

91 The cryogenic system is divided to an Outer Vessel (OV) which holds the insulation vacuum,  
 92 and an Inner Vessel (IV) which holds the xenon. In addition to the vacuum which prevents heat  
 93 leakage due to diffusion and convection, the IV is completely covered by multi layer Aluminized  
 94 Myler to prevent heating via radiation.

95 The OV is made of a 10" Conflat (CF) cube, with ports on all six faces, interfacing the gas  
 96 handling system and the detector part, and bearing service ports (e.g., feed-throughs, pumping

<sup>1</sup>N143 SN.12E AC 230V50HZ KNF diaphragm circulation pump

<sup>2</sup>GEA GBS100M-24 plate heat exchanger

<sup>3</sup>MONO-TORR PS4-MT15-R-2

<sup>4</sup>MKS mass flow controller 1179A00614CR1BM

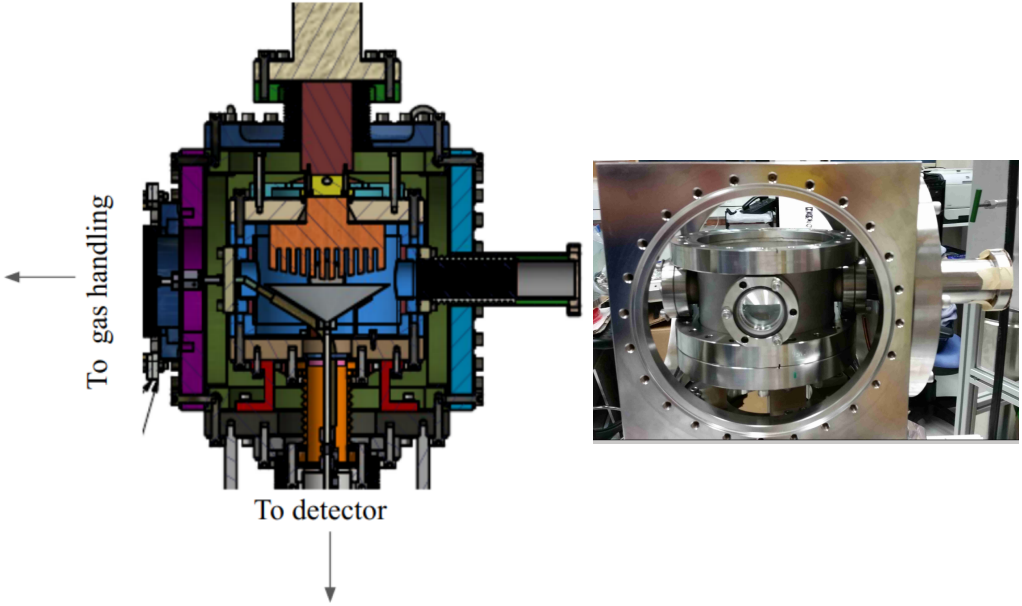


**Figure 4.** CAD view of the cryogenic system(Left) and a picture of the cryogenic system (Right) . The cryogenic system. (Left) CAD design view, (right) picture of the actual system.

97 ports, view ports). The OV is connected to the detector part via a 6" CF flexible bellows, providing  
 98 a shared vacuum.

99 The IV is made of 1.5" long cylinder with 6" CF flanges on both sides, holding xenon within.  
 100 A 120 mm diameter cold finger is welded to its top flange. The design of the cold finger is similar  
 101 to the one in [12]. The inner part of the cold finger is made of long fins, resulting in a better heat  
 102 transport. The upper part of the cold finger is in thermal contact with the QDrive cryo-cooler <sup>1</sup> via  
 103 a copper adapter. The copper adapter holds two  $100\Omega$  pt resistor<sup>2</sup> which are connected to a PID  
 104 reader<sup>3</sup> for temperature measurements. A cartridge-heater is also inserted to the copper adapter for  
 105 emergency heating in case xenon freezes on the cold finger.

106 The cryo-cooler is connected via a 4½" flange to the OV top flange. While usually cryo-  
 107 coolers used for xenon experiments constantly operate in maximal cooling, the QDrive cryo-cooler  
 108 utilizes a temperature control to vary its cooling power up to  $\sim 70$  W. This allows setting a desired  
 109 working temperature which is constant within less than  $0.1$  °C measured on the cryo-cooler.

110 On the inner side of the IV bottom flange a thin 0.6 mm Stainless Steel (SS) funnel is installed  
 111 collecting LXe drops from the cold finger, and delivering them to the detector. This flange is  
 112 attached to the detector part, via a 3⅓" flexible bellows. The bellows hosts two pipes connected  
 113 to the circulation system, and a third pipe coming from the funnel. The three pipes deliver LXe  
 114 whereas the GXe is filling the bellows volume. The purer LXe (from the gas handling system) and  
 115 the less pure LXe (from the cold finger) are separated, and can be delivered to different parts of the  
 116 system. Some of the guidelines for the design of the cryogenic system are based on [? ]. The CAD  
 117 view of the design of the cryogenic system and a photo of the actual system are shown in Fig 4.

<sup>1</sup>QDrive 20BB 9p6 A 3 AYNBNCO

<sup>2</sup>PT111 Lakeshore

<sup>3</sup>cryo-con model 18i Cryogenic Temp Monitor

### 118 2.3 The Detector System

119 The detector system refers to a vacuum chamber and its inner assembly consisting of a transparent  
 120 sphere that contains the LXe, the PMT sensors observing it and their accessories. This chamber is  
 121 placed below the cryogenic system.

122 The interface unit to the cryogenic system is built out of two flanges welded together via seven  
 123 tubes, which serve as service ports for electrical and other feedthroughs: four with a  $2\frac{3}{4}$ " CF flange,  
 124 and three with a  $1\frac{1}{3}$ " CF flange (mini-CF). The upper flange, ISO-K NW320, shares the cryogenic  
 125 system's OV insulation vacuum, while the bottom one, CF-10", is part of the IV and could hold  
 126 xenon for future detectors. The CF flange is also adapted to fit a smaller CF- $4\frac{5}{8}$ " flange which is  
 127 currently used.

128 The vacuum chamber is made of an ISO-K NW320 nipple closed with a blank flange from  
 129 below, the length of the nipple is determined such that the maximal height of the whole apparatus  
 130 is 190 cm, allowing an easy transport of the detector through standard doors.

131 The  $4\frac{5}{8}$ " CF flange is connected to a split vessel that serves as a LXe reservoir. one part is  
 132 connected to the top of the HPFS sphere, and one to the bottom. LXe is circulated such that LXe  
 133 coming from the gas system drips into one part and pumped from the other. This controls the liquid  
 134 level, and the sphere is constantly filled with LXe.

135 The sphere is a custom designed hollow shell made of Corning HPFS 8655 with high trans-  
 136mittance to VUV. Two Invar tubes with SS mini-CF flange are connected to the sphere on both  
 137 sides. The technical design and photo of the sphere are shown in Fig. 5. The optical properties  
 138 of the sphere will be further discussed in Sec. 3. The bottom flange of the sphere is held using a  
 139 brass holder to prevent force or torque applied on the sphere while mounting it. The brass holder  
 140 is connected to a plate held from the top CF-10" flange.

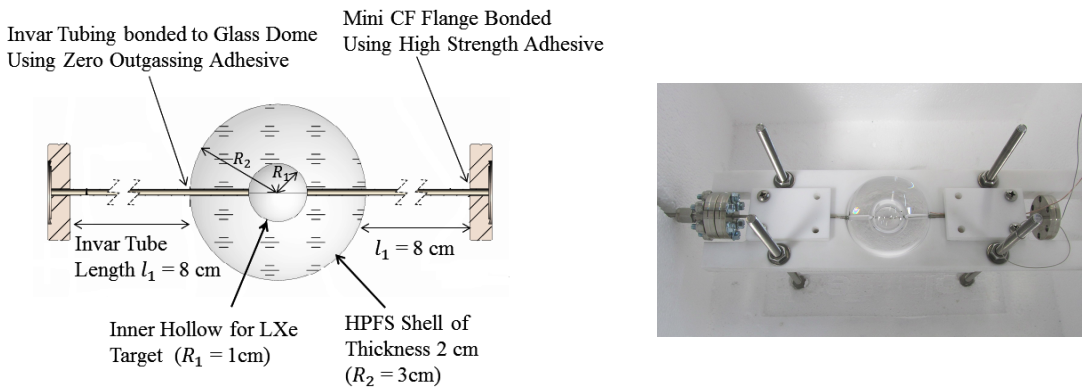


**Figure 5.** (Left)The technical design of the HPFS shell with Invar tubing and mini CF flanges. (Right) The industrially manufactured HPFS shell, held in a test fixture.

141 Photons emitted from the LXe in the sphere are detected by 20 PMTs<sup>1</sup>. The PMTs are chosen  
 142 to have a quantum efficiency greater than 30% at 178 nm. The voltage applied on each PMT  
 143 (the maximum is +900V) is adjusted such that the gain of the PMT is  $2 \times 10^6$ . A positive voltage

<sup>1</sup>R8520-406 Hamamatsu 1" PMT, active area 20.5 mm  $\times$  20.5mm

144 divider<sup>1</sup> is used to provide high voltage to the PMTs. The PMTs are held with a special aluminum  
 145 holder, coated with anti-reflection color. The holder is made of two hemispheres hosting the PMTs  
 146 in 3 rows, all of them pointing to the center of the sphere. The PMTs are attached to the holder by  
 147 their voltage–divider bases using M2 PEEK screws (see Fig 6). The CAD design and a photo of  
 148 the detector system are shown in Fig. 7.

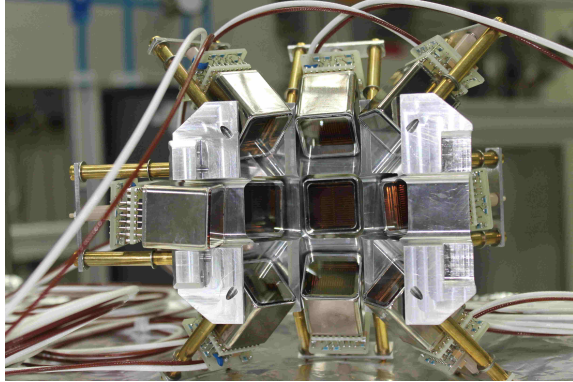


**Figure 6.** A PMT holder–hemisphere. Two identical hemispheres are used to hold the PMTS around the sphere.

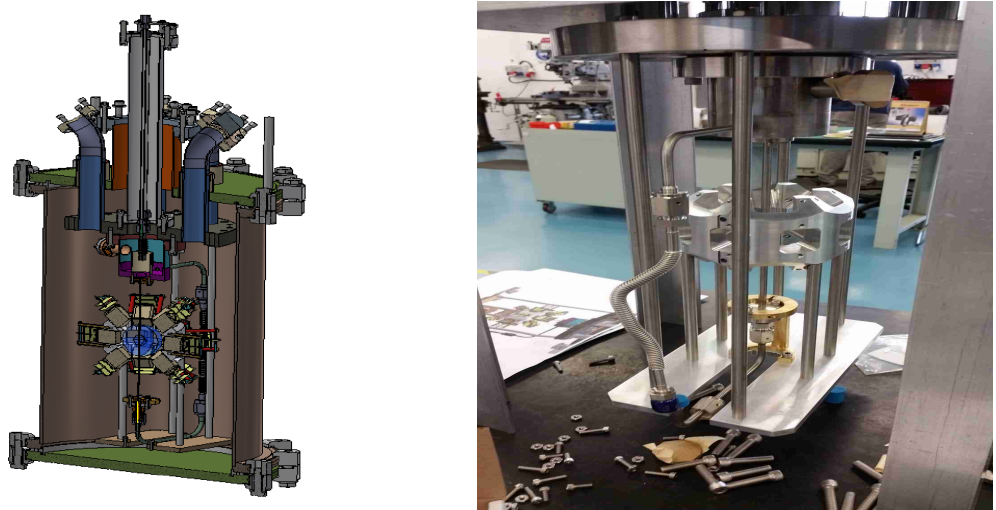


**Figure 7.** (Left) CAD design of the detector part. (Right) First mounting of the detector part, still not connected to the rest of the system.

#### 149 **2.4 The data acquisition system**

150 The DAQ system is heterogeneous using both NIM and VME electronic modules. The data readout  
 151 is being carried out through a PCIe card <sup>2</sup> connected via an optical link to a VME controller<sup>3</sup>. A  
 152 schematic layout of the DAQ system is shown in Fig. 8.

<sup>1</sup>Hamamatsu VDS18130p 24 channel positive polarity.

<sup>2</sup>CAEN A3818 PCIe

<sup>3</sup>CAEN V2718 VME controller

153      The PMTs are ramped up to their individual working voltage (corresponding to a gain of  
 154       $2 \times 10^6$ ) using VME high voltage distributor module<sup>1</sup>. The raw pulses from the PMTs are amplified  
 155      and shaped using two PMT preamplifiers<sup>2</sup>. The preamplifier operates from DC to 275 MHz and  
 156      produces two identical  $50\Omega$  non inverting outputs with voltage gains of 10 for each PMT channel.  
 157      One of the outputs is converted into a digital signal by an ADC<sup>3</sup>, and the other to binary signals  
 158      using two discriminators<sup>4</sup>.

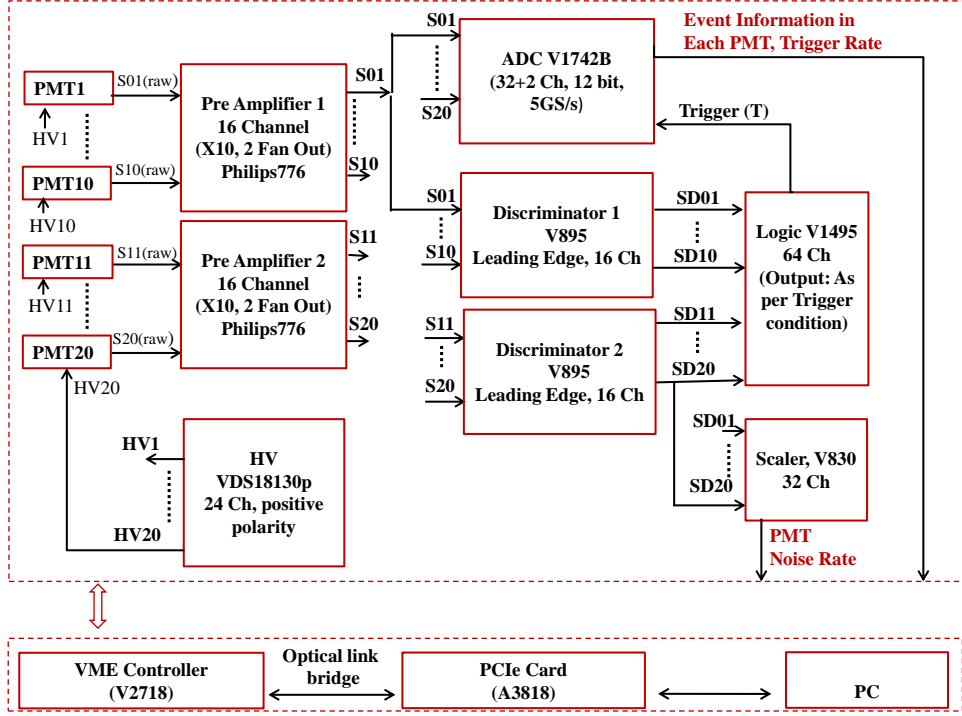


**Figure 8.** The schematic of the data acquisition system of DIREXENO. The signal coming from 20 PMTs ( $i = 1 - 20$ ) and the subsequent electronic channels to record the events once triggered. Where  $S_i(\text{raw})$  is the raw electrical pulse output of the PMTs,  $S_i$  are the amplified pulses, and  $SD_i$  are the binary outputs from the discriminator.

159      The ADC consists of two 12 bit 5 GS/s switched capacitor digitizer sections, each of them  
 160      with 16+1 channels, based on DRS4 chip. The dynamic range of the input signal is 1 Vpp with an  
 161      adjustable DC offset. This module constantly samples (5 GS/s, 2.5 GS/s or 2 GS/s) either bipolar  
 162      or unipolar analog input signals, and records them into circular analog memory buffers. Once  
 163      triggered, all analog memory buffers are frozen and digitized into a digital memory buffer with a  
 164      12 bit resolution. The measured rise time of the system (PMTs, bases, DAQ) is measured to be  
 165       $(1.4 \pm 0.6)$  ns, the measured jitter is,  $(390 \pm 67)$  ps.

166      The binary output signals from the discriminator are duplicated and fed to the logic module<sup>5</sup>

<sup>1</sup>iseg VDS18130p : 24 independent channels positive polarity voltage distributor

<sup>2</sup>Phillips 776. 16 independent and direct-coupled amplifiers channels

<sup>3</sup>CAEN ADC V1742: switched capacitor digitizer

<sup>4</sup>CAEN V895 16 channel leading edge discriminator

<sup>5</sup>CAEN V1495: FPGA based general purpose VME board

167 and to a scaler<sup>1</sup>. A global majority trigger is generated in the logic module with the coincidence of  
168 any two out of the twenty PMTs within a predefined time window, that will be optimized to reduce  
169 dark counts. The event information and trigger rate are read from the ADC, while the individual  
170 PMTs trigger rate from the scaler. Further analyses of the relevant events are carried out offline.

171 **2.5 The slow control system**

172 **3 Optical Properties of the Sphere**

173 The central component of the experiment is the HPFS sphere, which holds the LXe target, located  
174 in the center of the detector system. In order to allow the measurement of the original direction of  
175 photons emitted by the LXe, it is important to reduce the amount of diffractions and absorptions of  
176 photons on their path from the LXe to the PMTs.

177 To insure the photons emitted by the LXe can be measured by the PMTs, the HPFS trans-  
178 parency to VUV photons is crucial parameter for setting the sphere's dimensions (inner and outer  
179 radii). Therefore, the transmittance of an HPFS sample was measured, using the above mention  
180 VUV monochromator. The deuterium light source<sup>2</sup> spectrum is in the range of (110-190) nm,  
181 peaked at 160 nm was facing a vacuum space. Using a PMT placed in the vacuum, the intensity of  
182 the light is measured, both with and without the HPFS sample. The ratio of the measured intensities  
183 is converted to the transmittance of the HPFS. The transmittances as a function of wavelength are  
184 shown in Fig. 9 (right panel). The transmittance of the sample at 178 nm, is ~ 98.7 %/cm.

185 In order to reduce the diffraction in the LXe-HPFS transition, the sphere material is chosen  
186 to be HPFS, as the refractive index of it HPFS is 1.58 at 185 nm, matching to the LXe one, which  
187 is 1.61. The refractive index of this HPFS is 1.58 at 185 nm, matching to the LXe one, which is  
188 1.61. The refractive index at various wavelengths was measured in Prof. Amos Breskin's lab using  
189 a VUV monochromator<sup>3</sup>. The results of this measurements are shown in Fig. 9 (left panel). The  
190 sphere is made of two HPFS hemispheres bonded together.

191 Finally, in order to reduce the diffraction in the HPFS-Vacuum transition as well as internal  
192 reflections, the sphere should be thick so all photons will arrive in a perpendicular angle to the  
193 HPFS surface. In addition the sphere must not be too thick not to attenuate the scintillation light.  
194 The LXe target bubble within should be large to increase the detector medium but not be too large  
195 in order to avoid double scatters. Using a GEANT4 based simulation [13] studying the path of the  
196 scintillation photons the sphere dimensions are optimized. The outer radius is chosen to be 3 cm,  
197 and the inner (the hollow space that holds the LXe) is chosen to be 1 cm.

198 The sources that will be used for exciting the xenon and creating the superradiance (signal)  
199 as well as the standard emission (background), will be  $^{137}\text{Cs}$  ( $E_{\gamma}=662 \text{ keV}$ ) and  $^{57}\text{Co}$  ( $E_{\gamma}=122 \text{ keV}$   
200 & 136 keV) for ER with mean free path of ~ 4 cm and ~ 1 cm respectively. For NR,  $^{241}\text{AmBe}$ ,  
201 D-D neutron generator, or neutron produced in an accelerator will be used.

---

<sup>1</sup>CAEN V830: 16 channel scalar

<sup>2</sup>McPherson 632

<sup>3</sup>McPherson 234/302VM

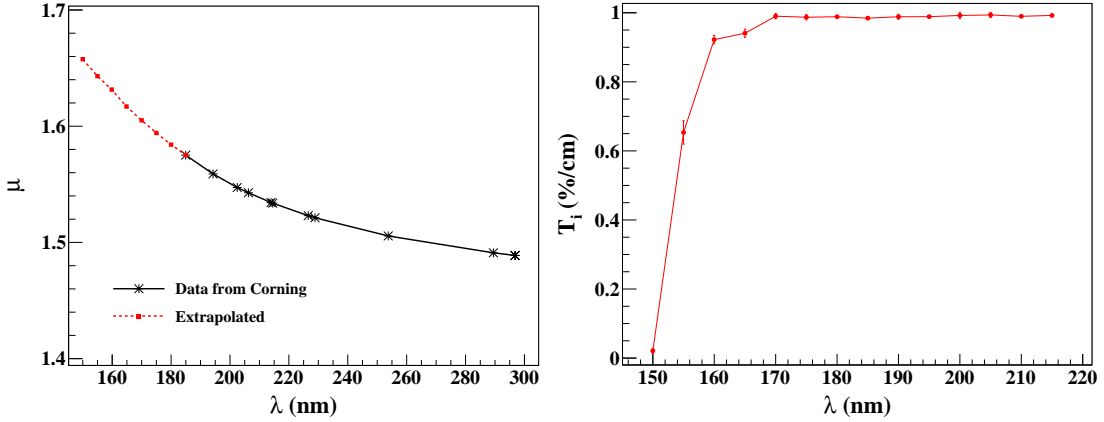


**Figure 9.** Some relevant characteristics of HPFS-8655. (Left) The refractive index as provided by corning and extrapolated to relevant wavelength range. (Right) The measured internal transmittance ( $T_i$ ), the mean and RMS obtained from 10 sets of measurements are shown.

## 202 4 Detector sensitivity

203 The sensitivity of the detector is estimated by its ability to identify an anisotropic component in the  
 204 scintillation photons emission pattern (signal), over the isotropic one (background). The photon  
 205 emission pattern is modeled using a combination of isotropic emission and one or two beams

$$\mathcal{F}(\theta, \phi) = (1 - r_{aniso}) \cdot f_{iso} + r_{aniso} \cdot [r_1 f_G(\sigma_1) + r_2 f_G(\sigma_2)], \quad (4.1)$$

206 where  $f_{iso}$  is the PDF of an isotropic emission,  $f_G$  is a PDF of a Gaussian distribution with half  
 207 width  $\sigma$ .  $r_{aniso}$  is the anisotropic emission fraction, and  $r_{1,2}$  are the relative beams intensities. The  
 208 first beam direction is random, and the second's is either random (“uncorrelated”) or opposite to  
 209 the first's (“correlated”). The different emission patterns used here are summarized in Table ??.

Pattern no.	No. of beams	type	Beam half widths		Signal fractions		$N'$
			$\sigma_1$	$\sigma_2$	$r_1$	$r_2$	
1	1	single beam	$5^0$	-	1	0	3200
2	1	single beam	$15^0$	-	1	0	4630
3	2	correlated	$5^0$	$5^0$	0.5	0.5	4520
4	2	correlated	$15^0$	$15^0$	0.5	0.5	9770
5	2	uncorrelated	$5^0$	$5^0$	0.5	0.5	9370
6	2	uncorrelated	$5^0$	$10^0$	0.5	0.5	19500
7	2	uncorrelated	$15^0$	$15^0$	0.5	0.5	28200
8	2	uncorrelated	$10^0$	$30^0$	0.5	0.5	49900
9	2	uncorrelated	$10^0$	$30^0$	0.2	0.8	56000
10	2	uncorrelated	$30^0$	$10^0$	0.2	0.8	43000

**Table 1.** Anisotropic emission patterns. For all patterns  $r_{aniso} = 0.1$

210 A GEANT4 based simulation is used to model the detector system, generate photons, propa-  
 211 gate them through the detector, and obtain a PMT hit pattern. The photons detected at the PMTs

212 are mapped and put through a statistical test to check the detector's sensitivity towards the different  
 213 emission patterns [? ].

214 The relevant geometrical and optical parameters, which are used in the simulation, are listed  
 215 in Table ?? . The scintillation light produced in a particular event is emitted by a cloud of excimers.  
 216 This cloud is assumed to have a linear size much smaller than that of the optical system. Therefore  
 217 each event is simulated as a number of photons that are emitted from a point in the LXe with some  
 218 emission pattern (see Table ?? ). The number of generated photons for each event is taken to be  
 219 Poisson(50), which correspond to an energy deposition of  $\sim 2.5\text{keV}$  or  $\sim 7\text{keV}$  for ER or NR  
 220 respectively. The LXe target is much smaller than the mean free path of the source particles, and to  
 221 account for that the events are uniformly generated in the LXe volume. The probability for a photon  
 222 being transmitted/reflected at a given surface is determined by Fresnel's equations, which include  
 223 Snell's law for the transmitted light, and specular reflection for the reflected light. The boundary  
 224 surfaces between different media such as, the LXe–HPFS, HPFS–vacuum and vacuum–PMT, are  
 225 assumed to be perfectly smooth, therefore enabling only specular reflection. The photons reaching  
 226 the PMTs can either be detected, absorbed or reflected from the photocathode or PMT window. A  
 227 simplified approach of the above possibilities is considered: a photon reaching the PMT has a 30%  
 228 probability to be detected (since the PMTs have  $\text{QE} \geq 30\%$ ), 50% probability to get absorbed and  
 229 20% probability to get specularly reflected.

Parameter	Value	Parameter	Value
LXe absorption length	100 cm	HPFS shell inner radius	1cm
LXe scattering length	35 cm	HPFS shell thickness	2 cm
LXe refractive index	1.61	PMT QE	30%
LXe Scintillation wavelength	178	PMT distance from center	39 mm
HPFS absorption length	100 cm	Number of PMT	20
HPFS refractive index	1.57	PMT active area	22mm $\times$ 22mm
HPFS scattering length	$\infty$	Invar tube diameter	1 mm

Table 2. The parameters used in simulation

230 The statistical fluctuation in the electronic signal generated in a PMT for a certain number of  
 231 incident photon is taken into account. The R8520 PMTs have 20% probability for double photo-  
 232 electron emission for 178 nm photons, which is included in the simulation. Each detected photon  
 233 on a PMT is assigned a uniform position on the PMT surface. The direction of this point with  
 234 respect to the center of the LXe sphere is defined as the incident direction of the photon. The di-  
 235 rection information is then used to calculate the angles between all possible pairs of photon for any  
 236 event and calculate the correlation between all angle pairs.

237 In order to quantify the anisotropy of the emission, the angle correlation distribution of an  
 238 anisotropic hit pattern is compared to that of the isotropic pattern. A  $\chi^2$  test statistic is used where  
 239 the reduced  $\chi^2$  is defined as

$$\chi^2_\nu = \frac{1}{\nu} \sum_{i=1}^{\nu} \frac{(O_i - E_i)^2}{E_i}, \quad (4.2)$$

240 where  $E_i$  is the expected number of entries for an isotropic emission obtained from a sample of  
 241  $10^5$  simulated events.  $O_i$  is the observed number of entries, and  $\nu$  is the total number of angle  
 242 correlation bins which is also the number of dof . Sixty bins of identical width are used.

243 To asses the needed exposure to claim discovery assuming one of the patterns mentioned  
 244 above,  $10^4$  data sets are generated and tested against the null hypothesis. This is repeated for  
 245 increasing number of events between 1 – 4000 assuming different values of the anisotropy fraction  
 246 ( $r_{aniso}$ ). The  $\langle \chi^2_\nu \rangle$  and its  $2\sigma$  band for pattern 1, assuming  $r_{aniso} = 0.1$  overlaid with the  
 247 corresponding values for an isotropic emission are shown in Fig. 10. The values of  $N'$ , required to  
 248 claim  $5\sigma$  discovery, for different values of  $r_{aniso}$  are calculated for each pattern as illustrated in  
 249 Fig. 11. The number of events  $N'$  for  $r_{aniso} = 0.1$  are summarized in Table ?? for all emission  
 250 patterns.

251 A simulation with two typical sources that emit isotropically, a  $10 \mu\text{Ci}$   $^{137}\text{Cs}$  (662 keV gamma),  
 252 and a  $2.7 \mu\text{Ci}$  AmBe ( 5 MeV neutron), shows that for an average yield of produced 50 photons/event,  
 253 the rate of events in the detector is:  $1.25 \times 10^4$  events/day for NR and 625 events/day for ER. There-  
 254 fore a system that can operate stably for few weeks is expected to do reasonable measurements for  
 255 ER and NR events.

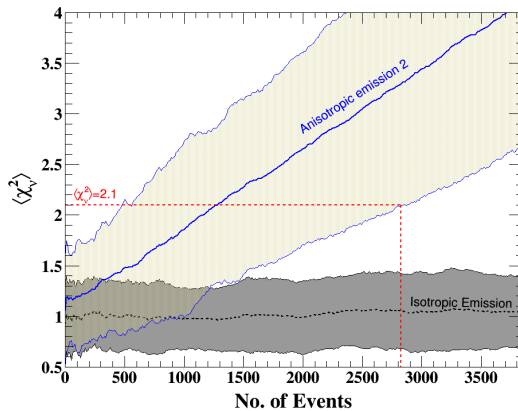


**Figure 10.**  $\langle \chi^2_\nu \rangle$  and its  $2\sigma$  band for isotropic emission (black) and for pattern 2 (blue). The  $\langle \chi^2_\nu \rangle$  for isotropic emission fluctuate around 1 with  $\sigma = 0.2$  which is consistent with the expected value of  $\frac{1}{\sqrt{30}} \equiv 0.18$  for reduced  $\chi^2$  distribution with 60 degrees of freedom.  $\sim 3000$  events are needed to claim  $5\sigma$  discovery ( $\chi^2_\nu = 2.1$ ) for this emission pattern

## 256 5 Commissioning runs

257 explain here what do we want show that we are able to do and why is it important.

258 In order for this system to be able to measure *superradiance* effects there are two important  
 259 features the system needs to meet: stability and fast response. The estimated time for accumulating  
 260 data to achieve a  $5\sigma$  effect assuming standard radioactive sources and some postulated

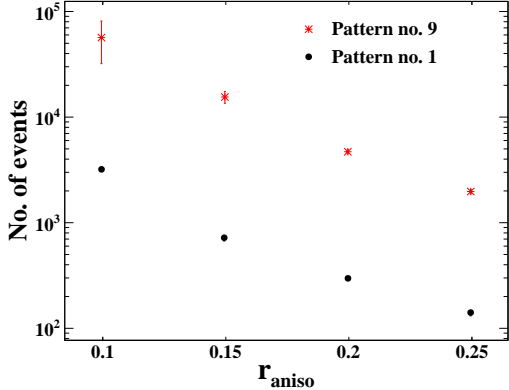


**Figure 11.** The number of events needed for an emission pattern to achieve  $5\sigma$  presented only for pattern 1 and 9, for different values of  $r_{\text{aniso}}$ .

261    **5.1 Stability Runs**

262    **5.2 Time resolution**

263    **6 Summary**

264    The setup of Direxeno, an experiment to measure the spatial and temporal distribution of LXe  
 265    scintillation, has been presented. The system consists of 4 main building blocks (gas handling,  
 266    cryogenic, detector, and DAQ), each of which can be exchanged without altering others allowing  
 267    significant flexibility and modularity. Each of the building blocks has been described in detail, with  
 268    emphasis on the design and components.

269    The sensitivity of the setup to different postulated non isotropic emission patterns are studied  
 270    using MC simulations. For the patterns studied, a run-time of 2-3 weeks is required using typical  
 271    radioactive sources. Therefore the system is designed to maintain stability over a reasonable time  
 272    period.

273    Using DireXeno, effects like superradiance or any other non-linear scintillation can be mea-  
 274    sured. Measuring the correlation between the direction of the emission and the direction of the  
 275    radioactive source, may lead to directionality measurement which will allow enhanced statistical  
 276    modeling of background and improved sensitivity in DM experiments.

277    **References**

- 278    [1] E. Aprile and T. Doke. Liquid Xenon Detectors for Particle Physics and Astrophysics. *Rev. Mod. Phys.*, 82:2053–2097, 2010.
- 280    [2] A. Rubbia. Future liquid Argon detectors. 2013. [*Nucl. Phys. Proc. Suppl.* 235-236, 190(2013)].
- 281    [3] J. Silk et al. *Particle Dark Matter: Observations, Models and Searches*. Cambridge Univ. Press,  
     Cambridge, 2010.
- 283    [4] E. Aprile et al. First Dark Matter Search Results from the XENON1T Experiment. 2017.
- 284    [5] D. S. Akerib et al. Results from a search for dark matter in the complete LUX exposure. *Phys. Rev. Lett.*, 118(2):021303, 2017.

- 286 [6] Changbo Fu et al. Spin-Dependent Weakly-Interacting-Massive-ParticleâŠNucleon Cross Section  
287 Limits from First Data of PandaX-II Experiment. *Phys. Rev. Lett.*, 118(7):071301, 2017.
- 288 [7] J. Aalbers et al. DARWIN: towards the ultimate dark matter detector. *JCAP*, 1611:017, 2016.
- 289 [8] R. H. Dicke. Coherence in spontaneous radiation processes. *Phys. Rev.*, 93:99–110, Jan 1954.
- 290 [9] M. Gross and S. Haroche. Superradiance: An essay on the theory of collective spontaneous emission.  
291 *Physics Reports*, 93(5):301 – 396, 1982.
- 292 [10] N G Basov, V A Danilychev, and Yurii M Popov. Stimulated emission in the vacuum ultraviolet  
293 region. *Soviet Journal of Quantum Electronics*, 1(1):18, 1971.
- 294 [11] Frederick H. Mies. Stimulated emission and population inversion in diatomic bound-continuum  
295 transitions. *Molecular Physics*, 26(5):1233–1246, 1973.
- 296 [12] E. Aprile et al. The XENON100 Dark Matter Experiment. *Astropart. Phys.*, 35:573–590, 2012.
- 297 [13] S. Agostinelli et al. Geant4 a simulation toolkit. *Nuclear Instruments and Methods in Physics*  
298 *Research Section A: Accelerators, Spectrometers, Detectors and Associated Equipment*, 506(3):250 –  
299 303, 2003.